HHS Public Access

Author manuscript

Ann Biomed Eng. Author manuscript; available in PMC 2022 December 01.

Published in final edited form as:

Ann Biomed Eng. 2021 December ; 49(12): 3465–3480. doi:10.1007/s10439-021-02884-y.

Patient-specific computational analysis of hemodynamics in adult pulmonary hypertension

Narasimha R. Pillalamarri[1], **Senol Piskin**[2], **Sourav S. Patnaik**[1,3], **Srinivas Murali**[4], **Ender A. Finol**[1,5,$]

[1]University of Texas at San Antonio, Department of Mechanical Engineering, One UTSA Circle, San Antonio, TX 78249

[2]Istinye University, Department of Mechanical Engineering, Istanbul, Turkey

[3]University of Texas at Dallas, Department of Bioengineering, Richardson, TX

[4]Allegheny Health Network, Division of Cardiovascular Medicine, Pittsburgh, PA

[5]University of Texas at San Antonio, UTSA/UTHSA Joint Graduate Program in Biomedical Engineering, San Antonio, TX

Abstract

Pulmonary hypertension (PH) is a progressive disease characterized by elevated pressure and vascular resistance in the pulmonary arteries. Nearly 250,000 hospitalizations occur annually in the U.S. with PH as the primary or secondary condition. A definitive diagnosis of PH requires right heart catheterization (RHC) in addition to a chest computed tomography, a walking test, and others. While RHC is the gold standard for diagnosing PH, it is invasive and posseses inherent risks and contraindications. In this work, we characterized the patient-specific pulmonary hemodynamics *in silico* for diverse PH WHO groups. We grouped patients on the basis of mean pulmonary arterial pressure (mPAP) into three disease severity groups: *at-risk* (18 $mmHg \leq mPAP < 25$ *mmHg*, denoted with *A*), *mild* (25 $mmHg \leq mPAP < 40$ *mmHg*, denoted with *M*), and *severe* ($mPAP \geq 40$ *mmHg*, denoted with *S*). The pulsatile flow hemodynamics was simulated by evaluating the three-dimensional Navier–Stokes system of equations using a flow solver developed by customizing OpenFOAM libraries (v5.0, The OpenFOAM Foundation). Quasi patient-specific boundary conditions were implemented using a Womersley inlet velocity profile and transient resistance outflow conditions. Hemodynamic indices such as spatially averaged wall shear stress (*SAWSS*), wall shear stress gradient (*WSSG*), time-averaged wall shear stress (*TAWSS*), oscillatory shear index (*OSI*), and relative residence time (*RRT*), were evaluated along with the clinical metrics pulmonary vascular resistance (*PVR*), stroke volume (*SV*) and compliance (*C*), to assess possible spatiotemporal correlations. We observed statistically significant decreases in *SAWSS*, *WSSG*, and *TAWSS*, and increases in *OSI* and *RRT* with disease severity. *PVR* was moderately correlated with *SAWSS* and *RRT* at the mid-notch stage of the cardiac cycle when these indices were computed using the global pulmonary arterial geometry. These results are promising in the context of a long-term goal of identifying computational biomarkers that can serve as surrogates for invasive diagnostic protocols of PH.

[$]Corresponding author: Tlf: (210) 458-8058, Fax: (210) 458-6504, ender.finol@utsa.edu.

3. INTRODUCTION

Pulmonary hypertension (PH) is a vascular condition characterized by high blood pressure in the pulmonary arteries, which typically affects 15 – 50 persons per million [1]. Currently, PH diagnosis requires multiple sessions of a six-minute walk test, trans-thoracic echocardiography, and right heart catheterization (RHC) [2]. While RHC is the gold standard for diagnosing PH, it is invasive and limits the cardiologist's ability to safely diagnose and monitor the disease. A definitive, non-invasive alternative for RHC would be of profound benefit for the clinical management of this disease. Efforts to develop non-invasive diagnostic methods have extensively characterized pulmonary hemodynamics using MRI-derived blood flow patterns [3], 4D MRI [4, 5], and computational fluid dynamics (CFD) modeling [6–10].

CFD simulations offer superior spatial and temporal flow resolutions, and the capability to resolve pathological hemodynamic challenges [11]. Nevertheless, modeling the hemodynamics in the adult pulmonary vasculature invariably requires certain reasonable approximations. Kheyfets *et al.* [6], Bordones *et al.* [12], and Tang *et al.* [13] used a rigid wall, no-slip boundary condition for the pulmonary arterial walls. At the inlet, the volume flow rate was constant in time and parabolic in space. These studies, albeit useful in gaining insights on the hemodynamics of PH, overlooked the contributions made by the compliant wall of the pulmonary vasculature. This limitation was resolved by coupling the hemodynamics with enclosing wall motion using fluid-structure interaction (FSI) simulations [14–18]. One FSI method involved a coupled-momentum model with the assumption of linearized stiffness for the arterial wall [16, 17, 19], while Gutierrez *et al.* [20] used small deformation theory. Su and colleagues [14, 15] employed idealized geometries.

A vast majority of modeling studies [6, 11, 12, 16–18, 21] have dealt with pulmonary arterial hypertension (PAH, WHO group I). However, left heart disease (WHO group II) and lung disease (WHO group III) are causative factors for PH in the majority of diagnosed cases [22]. In this work, we quantified the pulmonary hemodynamics in PH patients belonging to diverse WHO groups. We hypothesize that irrespective of WHO classification, pulmonary hemodynamics is strongly associated with PH disease severity. We also investigated the feasibility of using hemodynamic measures for developing a reliable non-invasive PH diagnosis protocol. In doing so, we attempted to address the following research questions:

1. Is disease severity highly associated with specific hemodynamic measures in PH patients?
2. If this association exists, is it affected by the spatiotemporal distribution of the hemodynamic measures?

4. METHODS

All abbreviations used in this manuscript are described in Table 1, which includes mathematical formulations used to calculate hemodynamic measures, if applicable.

Following Institutional Review Board approval at Allegheny General Hospital (Pittsburgh, PA), patient-specific geometries of the pulmonary vasculatures were reconstructed from standard of care chest CT angiography (CTA) images obtained retrospectively from 32 adult PH patients. Of these, three patients belonged to WHO group I, six to WHO group II, twenty to WHO group III, one to WHO group IV, and two patients' WHO group was unknown (see Table 2). Each patient underwent the electrocardiogram-gated chest CTA exam and RHC with a Swan-Ganz standard thermo-dilution catheter. Table 2 details the patient-specific clinical data collected or calculated during the retrospective review of medical records. In this investigation, we categorized the patients on the basis of disease severity following the recommendations described in Simonneau *et al*. [23] and Kolte *et al*. [24], as follows: *at-risk* ($18\ mmHg \leq mPAP < 25\ mmHg$, denoted with *A* in Table 2), *mild* ($25\ mmHg \leq mPAP < 40\ mmHg$, denoted with *M*), and *severe* ($40\ mmHg \leq mPAP$, denoted with *S*).

The simulation domain extends from the proximal MPA up to seven generations of branching pulmonary arteries. To avoid boundary-based instabilities, the inflow and outflow surfaces were extended ten times their hydraulic diameters. Figure 1a illustrates the simulation domain for an exemplary PH patient, whereas Fig. 1b shows a magnified view of the same reconstructed pulmonary vasculature. Each patient-specific domain was discretized with nearly 6.5 ± 1.5 million tetrahedral mesh elements in ICEM (Ansys Inc., Canonsburg, PA). Grid convergence studies were previously undertaken by monitoring changes in spatially varying instantaneous wall shear stress (WSS) [15]. The CFD solver was developed in-house by customizing open-source C++ libraries available in OpenFOAM (The OpenFOAM Foundation Ltd, London, U.K.) – v5.0 distribution. Robertson *et al*. [25], and the references therein, offer an impressive account of notable CFD-based studies conducted using OpenFOAM. Appendix A of the Supplementary Material provides additional details on the infrastructure for the CFD simulations and the governing equations used for them. Blood was considered an incompressible, Newtonian fluid. The finite volume formulation implemented in the solver evaluates the integral form of the incompressible Navier-Stokes system of equations. Appendix B of the Supplementary Material describes the experimental validation of computational results and third-party verification studies conducted for the OpenFOAM solver.

4.1 Inflow boundary conditions

Velocity and pressure waveforms were recorded in the proximal MPA for five adult PH patients with a ComboWire XT catheter. This subject group was separate from the one described in Table 2. The raw patient-specific velocity and pressure data were post-processed and normalized against cardiac output (*CO*) and mean pulmonary arterial pressure (*mPAP*), respectively. Dimensionless waveforms of velocity (see Fig. 2a) and pressure (see Fig. 2b) were evaluated against a normalized timescale.

Subsequently, quasi-patient specific inflow velocities were calculated for the 32 vascular models (Table 2) using their respective *CO* and *mPAP* as dimensional factors. A fully developed pulsatile velocity profile (according to the Womersley pulsatile flow solution) was used for the inflow boundary condition during one cardiac cycle. A protocol based on Schwartz–Christoffel mapping was implemented to specify the velocity values on the

non-circular inlets [26]. The simulations were run for three cardiac cycles to obtain periodic convergence.

4.2 Outflow boundary conditions

A resistance structured-tree outflow boundary condition, proportional to the respective outlet radius, was applied at each extended outlet boundary. We emulated the algorithm described in the work of Kheyfets *et al.* [6] to isolate a unique polynomial equation for each patient-specific geometry. For example, Eq. (1) defines the outlet resistances for the CFD model of patient No. 5,

$$\begin{aligned} R_i = & -\left(5.04\times10^5\right)r_i^7+\left(3.041\times10^6\right)r_i^6 \\ & -\left(7.582\times10^6\right)r_i^5+\left(1.009\times10^7\right)r_i^4 \\ & -\left(7.727\times10^6\right)r_i^3+\left(3.4\times10^6\right)r_i^2 \\ & -\left(8.028\times10^5\right)r_i+\left(8.136\times10^4\right) \end{aligned} \tag{1}$$

where R_i and r_i denote the resistance and radius at outlet i, respectively. In this work, we introduced a variable coefficient, α, to adjust the outlet resistances within each time iteration, as shown in Eq. (2),

$$R_i^{n+1} = \underbrace{\left[\frac{p_{wf}(t)}{p_{in}(t)}\right]}_{\alpha} R_i^n \tag{2}$$

where $p_{in}(t)$ is the inlet pressure at the current iteration, $p_{wf}(t)$ is the quasi-patient specific pressure obtained from the inlet pressure waveform described in section 4.1, and n is the inner iteration counter within a time iteration. The constant, α, is the same for the resistances of all outlets. A subroutine (see Fig. 3a) iteratively modifies α, and by extension, the outlet resistances within every time step until the condition expressed by Eq. (3) is satisfied.

$$0.99\ p_{wf}(t) \le p_{in}(t) \le 1.01\ p_{wf}(t) \tag{3}$$

The rationale for using this subroutine is to simultaneously achieve quasi-patient specific velocity and pressure at the inflow boundary. In addition, the subroutine yields the time-lag between pressure and velocity waveforms measured during RHC (see Fig. 3b). This time difference primarily exists on account of the inertia and viscosity of blood [27].

4.3 Hemodynamic Indices

The three dimensional flow fields were post-processed using ParaView (Kitware Inc., Clifton Park, NY). This consisted in quantifying the following hemodynamic indices for each pulmonary vasculature:

1. Spatially averaged wall shear stress (*SAWSS*):

$$SAWSS = \frac{1}{A}\int_A |\tau_w| dA \tag{4}$$

where τ_w is the wall shear stress (WSS) vector field computed as the tangential component of the traction on the luminal surface and A is the discretized vascular luminal area. The limited in-plane resolution of the CTA images results in isolated regions of the distal vasculature that yield non-physiological, high focal WSS. Based on the findings of Tang *et al.* [7], facets with WSS magnitude greater than 50 dyn/cm^2 were considered an anomalous product of the image resolution and thus were not included in the $SAWSS$ calculation. Increasing this threshold beyond 50 dyn/cm^2 revealed insignificant changes in $SAWSS$.

2. Wall shear stress gradient ($WSSG$):

$$WSSG = \sqrt{\left(\frac{\partial \tau_w}{\partial \xi}\right)^2 + \left(\frac{\partial \tau_w}{\partial n}\right)^2} \tag{5}$$

where ξ and n represent local tangential and normal directions to the luminal surface. The tangential direction comprises two in-plane components; the unit vector parallel to the resultant of these components was used to calculate the directional derivative of the WSS vector. The unit vector ξ retains the direction of the local instantaneous WSS vector.

3. Time averaged wall shear stress ($TAWSS$):

$$TAWSS = \frac{1}{T}\int_T |\tau_w| dt \tag{6}$$

where T represents the time period for one cardiac cycle, which is achieved in increments of time interval dt.

4. Oscillatory shear index (OSI):

$$OSI = \frac{1}{2}\left[1 - \frac{\left|\int_T \tau_w dt\right|}{\int_T |\tau_w| dt}\right] \tag{7}$$

5. Relative residence time (RRT):

$$RRT = \frac{1}{[(1 - 2 \times OSI) \times TAWSS]} \tag{8}$$

4.4 Statistical analysis

A one-way analysis of variance was performed to determine if statistically significant differences exist in the aforementioned hemodynamic indices among the three severity groups. This was followed by Tukey's multiple comparison tests to compare the simulation-based indices among all possible pairs of severity groups. A probability value less than 0.05,

i.e $p < 0.05$, was considered statistically significant. In addition, a Pearson's correlation analysis with Bonferroni correction was performed with all the calculated indices vs. the following clinical metrics: pulmonary vascular resistance (PVR), compliance (C), and stroke volume (SV). For this analysis, a probability value less than 0.01, i.e $p < 0.01$, was considered statistically significant.

5. RESULTS

5.1 Simulation-based hemodynamic indices

Figure 4 illustrates the $TAWSS$ distribution obtained for all the patient-specific geometries. Qualitatively, all patient-specific vasculatures exhibited elevated $TAWSS$ in the distal ends. We observed a concomitant reduction in regions with $TAWSS > 10\ dyn/cm^2$ in relation to the severity of the disease, i.e. with S vasculatures having the least number of regions with elevated $TAWSS$.

Figure 5 shows $SAWSS$ at peak systole (Figs. 5a, 5d, 5g, and 5j), mid-notch (Figs. 5b, 5e, 5h, and 5k), and mid-diastole (Figs. 5c, 5f, 5i, and 5l). To examine the regional dependence of $SAWSS$, the patient-specific geometries were divided into three regions: MPA, left and right pulmonary arteries (LR), and the distal vasculature (D), based on the Weibel system [28]. The spatial averaging is conducted globally (G), i.e. on the complete geometry, in addition to the aforementioned regions. In Figs. 5–7, peak systole is designated with the subscript PS, the mid-notch with the subscript MN, and mid-diastole with the subscript MD. All measures of $SAWSS$ demonstrated significant differences among the three groups, except $SAWSS_{MPA,MD}$. The mean $SAWSS_{G,PS}$ for the A group exceeded that of the M group by 14.5%, whereas $SAWSS_{G,PS}$ for the M group exceeded the S group by 36.3% (mean $SAWSS_{G,PS}$: 21.50 dyn/cm^2 (A), 18.37 dyn/cm^2 (M), 11.71 dyn/cm^2 (S), $p = 0.007$). The A and M groups exhibited less than 5% disparity for $SAWSS_{G,MN}$ ($p = 0.002$) and $SAWSS_{G,MD}$ ($p = 0.011$). However, the S group exhibited 37.9% lower $SAWSS_{G,MN}$ and 43.3% lower $SAWSS_{G,MD}$, compared to the M group. Figure 6 shows the percentage decreases computed in regionally averaged $SAWSS$ at the said time instants. $SAWSS_{MPA,PS}$, $SAWSS_{MPA,MN}$, $SAWSS_{MPA,MD}$, $SAWSS_{LR,PS}$, $SAWSS_{LR,MN}$, and $SAWSS_{LR,MD}$ yielded percentage deacreases in the range of 20–40%. However, in the distal vasculature, the percentage decreases for $SAWSS_{D,PS}$, $SAWSS_{D,MN}$, and $SAWSS_{D,MD}$ were small (< 5%) between the A and M groups, and large (30 – 45%) between the M and S groups.

$WSSG$ was calculated at PS, MN, and MD for each of the severity groups, as shown in Figs. 7a through 7l with global and regional spatial averages of $WSSG$. $WSSG_{MPA,MD}$, $WSSG_{LR,MN}$, $WSSG_{LR,MD}$, and $WSSG_{D,PS}$ did not exhibit any statistically significant differences among the severity groups. For all groups, the differences between $WSSG_{G,PS}$ ($p = 0.022$) and $WSSG_{G,MN}$ ($p = 0.009$) were less than 10%. $WSSG_{G,PS}$, $WSSG_{G,MN}$, and $WSSG_{G,MD}$ demonstrated significant pairwise differences between the M and S groups. Pairwise differences were also observed between the A and S groups for $WSSG_{MPA,PS}$, $WSSG_{MPA,MN}$, and $WSSG_{LR,PS}$. $WSSG$ in the distal vasculatures, i.e. $WSSG_{D,PS}$, $WSSG_{D,MN}$, and $WSSG_{D,MD}$, were found to be nearly double their counterparts in the MPA and LR regions.

Figure 8 illustrates the spatially averaged *TAWSS* distributions calculated for the three severity groups. $TAWSS_G$ showed pairwise statistical significance between the *A* and *S* groups, and the *M* and *S* groups (Fig. 8a, p = 0.002). $TAWSS_{MPA}$ was 40.0% lower (*A* vs. *M*) and 34.4% lower (*M* vs. *S*) (Fig. 8b, p = 0.011). Similar trends were observed for $TAWSS_{LR}$ with decreases of 34.0% (*A* vs. *M*) and 41.3% (*M* vs. *S*) (Fig. 8c, p = 0.010). Collectively, $TAWSS_D$ was the highest amongst all groups (Fig. 9d, p = 0.008), whereas $TAWSS_{MPA}$ was observed to be the lowest.

OSI represents a fusion of the low and oscillatory shear theories into a single, nondimensional measure of WSS relevant for regions of the vasculature with significant flow reversal. Figure 9 shows the spatial averages of *OSI*. OSI_G increases concomitantly with disease severity: *A* (0.047 ± 0.02), *M* (0.053 ± 0.006), and *S* (0.060 ± 0.021), although the differences between the groups were statistically insignificant ($p = 0.231$), as shown in Fig. 9a. Similar increases were obtained for OSI_{MPA} (Fig, 9b, $p = 0.033$) between the *A* (0.109 ± 0.021) and *M* (0.160 ± 0.017) groups, and a decrease from the *M* to the *S* group (0.148 ± 0.054). No statistically significant differences were obtained amongst the severity groups for OSI_{LR} and OSI_D (Figs. 9c and 9d). For all severity groups, the mean *OSI* follows the inequality $OSI_{MPA} > OSI_{LR} > OSI_D$, suggesting attenuation of the flow pulsatality in the downstream direction.

RRT is a measure used to characterize near-wall stagnation. Figure 10 shows the spatially averaged normalized *RRT* for each severity group, where the normalization is with respect to the maximum *RRT* amongst the 32 CFD models. All spatial averages demonstrated statistically significant differences for the three severity groups. The normalized RRT_G, RRT_{MPA}, and RRT_{LR} were highest for the *S* group and lowest for the *A* group (Figs. 10a – 10c; $p = 0.006$, $p = 0.029$, and $p = 0.027$, respectively). However, in the distal vasculature, the lowest normalized RRT_D was obtained for the *M* group: *A* (0.186 ± 0.022), *M* (0.148 ± 0.005), and *S* (0.425 ± 0.015), as shown in Fig. 10d ($p = 0.008$).

5.2 Correlations between hemodynamic indices and clinical metrics

The association between the simulation-based indices and clinical metrics (*PVR*, *C*, and *SV*) was investigated by means of linear regression analysis. Pearson's correlation coefficients, with Bonferroni correction, were calculated for all possible pairs of hemodynamic indices and clinical metrics. Tables 3 and 4 describe the statistically significant ($p < 0.01$) Pearson's correlation coefficients between *SAWSS* and *WSSG*, and the clinical metrics; no other time-dependent hemodynamic indices yielded statistically significant correlations. Tables 5 and 6 illustrate the significant associations between *TAWSS* and *RRT*, and the clinical metrics; no other time-averaged hemodynamic indices yielded statistically significant correlations. *PVR* correlated significantly with all time-dependent indices except $WSSG_{MPA,PS}$, $WSSG_{MPA,MD}$, $WSSG_{D,PS}$, and $WSSG_{D,MD}$. Moreover, moderate correlations (ρ) were observed for *PVR* with $SAWSS_{G,MN}$ ($\rho = -0.67$), $SAWSS_{G,MN}$ ($\rho = -0.67$), $SAWSS_{D,MN}$ ($\rho = -0.62$), $TAWSS_G$ ($\rho = -0.62$), RRT_G ($\rho = 0.68$), RRT_{LR} ($\rho = 0.67$), and RRT_D ($\rho = 0.65$). *C* weakly correlated with $SAWSS_{D,MN}$ ($\rho = 0.50$), while it yielded either insignificant correlations or correlations with $|\rho| < 0.50$ with all other indices. *SV* had moderate correlations with $SAWSS_{MPA,MD}$ ($\rho = 0.63$) and $SAWSS_{LR,MD}$ ($\rho = 0.62$).

Its associations with other indices ($SAWSS_{G,PS}$, $SAWSS_{LR,PS}$, $WSSG_{G,PS}$, $WSSG_{D,PS}$, $SAWSS_{D,PS}$) were insignificant ($p > 0.01$) or weak ($|\rho| < 0.5$).

6. DISCUSSION

In the present work, we developed patient-specific pulmonary aterial models for a group of 32 adult PH patients classified as (*A*) at-risk (18 $mmHg \leq mPAP < 25$ $mmHg$), (*M*) mild (25 $mmHg \leq mPAP < 40$ $mmHg$) and (*S*) severe ($mPAP \geq 40$ $mmHg$). Each patient's chest CTA images were segmented to obtain the pulmonary endoluminal boundary followed by 3D reconstruction of the patient-specific vasculature. The distal regions of the vasculature extended up to seven generations of branching pulmonary arteries. Pulsatile blood flow simulations were completed by means of an in-house CFD solver using quasi-patient specific inflow/outflow boundary conditions that achieved the $mPAP$ measured at the proximal MPA during RHC. From these, we computed six hemodynamic indices and interrogated their potential association with three standard of care clinical metrics indicative of PH prognosis.

Five hemodynamic indices were derived from the spatiotemporal distribution of WSS. Multiple investigations have been reported on the use of WSS magnitude [6], direction [29], gradients [30, 31], and topological features [29, 32, 33] to characterize arterial hemodynamics. To this end, we calculated $SAWSS$ at three salient stages of the cardiac cycle (peak systole, mid-notch, and mid-diastole). The mild patient group exhibited a $SAWSS$ lower than that of the at-risk group for the three stages at the MPA, LR, and D regions, although such differences were statistically insignificant. Conversely, the lower $SAWSS$ obtained for the severe group was statistically significant compared to the mild group. Noteworthy is that the percentage differences in $SAWSS$ for the distal vasculature comparing the severe and mild groups were at least 6 times larger than the corresponding differences between the mild and at-risk groups. We infer from this outcome that low WSS at peak systole, mid-notch, and mid-diastole could be a consequence of PH disease severity. Such concomitant decrease in $SAWSS$ with disease severity is in agreement with previous CFD studies [6, 7] and MRI-based measurements [4, 34, 35] in the pulmonary vasculature with PH. A similar result was obtained for the $WSSG$ prediction of the global pulmonary geometry, where groupwise differences and the mild vs. severe group differences were statistically significant at the three stages of the cardiac cycle. $WSSG$ decreased with disease severity irrespective of spatiotemporal location, although pairwise group differences were not significant. Flow through complex and tortuous blood vessel geometries results in significant spatial variations of WSS and local vortex structures [36]. $WSSG$ is a hemodynamic measure used to explain flow-induced arterial wall pathology and morphological changes in the intima [30]. It is believed that sustained hemodynamic abnormalities, explained in part by $WSSG$ distributions, may bring irreversible changes to the endothelium.

$TAWSS$ reflected the inter-group variations in a pattern similar to $SAWSS$ and $WSSG$ for the global and regional distributions. For the global pulmonary geometry, groupwise differences and the mild vs. severe group differences were statistically significant. Analogous to $SAWSS$ and $WSSG$, $TAWSS$ decreased with disease severity and increased

distally. *OSI* accounts for the temporal oscillations in WSS magnitude. An increase in *OSI* is often accompanied by a reduced *TAWSS* and together they provide evidence of abnormal hemodynamics on account of either arterial remodeling or vascular injury [37]. *OSI* increased with disease severity and decreased distally. This may be explained in part by the more evident flow separation in the MPA leading to elevated fluctuations in flow directionality, which become diminished in the distal vasculature. However, we observed statistical significance of *OSI* only within the MPA and for the pairwise relationship between the at-risk and mild groups. Yang *et al.* [8] reported similar results for pediatric PH patient groups. In an MRI-based study of 5 adult PH patients, Terada *et al.* [5] reported OSI_{MPA} = 0.214 ± 0.026, which is 47% higher than the *OSI* we obtained in this work (OSI_{MPA} = 0.146 ± 0.041). This difference could be attributed to the methods used for MRI data acquisition, the limited resolution for near-wall flow characteristic of MRI, and the small number of participants. Our CFD simulations lack individual inflow velocity profiles and are based on a rigid wall assumption, which can also explain the discrepancies in OSI_{MPA} relative to [10]. Regions with low *TAWSS* and high *OSI* experience large *RRT*, which is indicative of nearly stagnant blood flow. Lee *et al.* [38] proposed using *RRT* to characterize low and oscillatory shear. Elevated *RRT* can also signify constriction or obstruction within a blood vessel, and has been used as a strong indicator of thrombus formation in aneurysms [36, 39]. To the best of our knowledge, our study is the first to investigate *RRT* as an indicator of a progressing PH condition. We observed an increase in normalized *RRT* with disease severity and the groupwise differences were statistically significant for the global and regional distributions. The higher mean *RRT* in the distal vasculature suggests a more steady and unidirectional flow in the small pulmonary branches compared to the MPA.

One of the objectives of this investigation was to examine the potential relationship between simulation-based hemodynamic indices and clinically measured or calculated metrics. The statistical correlations, described in Tables 3 and 4, proved to be dependent on the space and time windows in which the indices were evaluated. The global spatial averages of the indices were predominantly predicted by the values in the distal vasculature. Moderate correlations were obtained between *PVR* and most indices. The time-dependent indices (*SAWSS* and *WSSG*) demonstrated relatively strong associations with *PVR* and *SV* at the mid-notch. The highest correlation coefficient for these indices was obtained for $SAWSS_{G,MN}$ vs. *PVR* ($\rho = -0.67$). The time-averaged indices (*TAWSS*, *OSI*, and *RRT*) demonstrated relatively strong associations with *PVR*, with the highest correlation coefficient found between RRT_G and *PVR* ($\rho = 0.68$). We infer from this outcome that a clinical relevant measure such as *PVR*, which is used for PH diagnosis and patient follow up, can be predicted with global WSS-derived metrics, such as *SAWSS* and *RRT*, when calculated from *in silico* models of the pulmonary vasculature. Our hypothesis was partially proven in that pulmonary hemodynamics, when quantified by means of *SAWSS*, *WSSG*, *TAWSS*, *OSI*, and *RRT*, is strongly associated with PH disease severity if using *in silico* models of the global pulmonary geometry.

Our work is subject to several important limitations. The relatively low number of patients in each disease severity category with no corresponding control group is one such limitation. The absence of control subjects can be explained in part by the difficulty of exposing healthy individuals to a redundant RHC procedure that they do not need. The available

patient-specific data for each severity group restricted our ability to postulate a universally applicable hypothesis on the existence of non-invasively diagnosable disease markers. To this end, a follow up computational study with a larger patient population is warranted. The CFD simulations assumed the blood to be a continuum and Newtonian fluid. Though Arzani *et al.* [40] provided a strong justification in favor of a Newtonian fluid assumption, blood is inherently a colloidal medium. Therefore, a particulate flow simulation with Lagrangian tracking would provide a superior model for pulmonary blood flow simulations. Furthermore, our CFD simulations assumed rigid wall boundaries, which might have led to an overestimation of the regional shear stress distributions. In the absence of vessel compliance, all the pulse pressure energy is transferred to the distal vessels and the reactive component of impedance in the flow dynamics is neglected. The lack of available patient-specific inflow and outflow boundary conditions is a formidable hurdle in studies such as ours. We were successful in partially overcoming this obstacle by means of quasi-patient specific boundary conditions calculated from clinical measurements obtained during RHC. Nonetheless, we acknowledge the limitation of lacking individual velocity and pressure profiles as boundary conditions to match the patient-specific geometries. To this end, a longitudinal study that quantifies changes in MPA diameter with disease progression would be valuable, as such changes would likely result in variations in the inlet velocity waveform used for the CFD simulations.

Spatiotemporal localization of simulation-based hemodynamic indices representative of pulmonary arterial blood flow in adult PH proved to be a valuable method for identifying the inter-group variations of such indices. We observed statistically significant decreases in *SAWSS*, *WSSG*, and *TAWSS*, and increases in *OSI* and *RRT* with disease severity. *PVR* was moderately correlated with *SAWSS* and *RRT* at the mid-notch stage of the cardiac cycle when these indices were computed using the global pulmonary arterial geometry. Regional distributions of these indices for the MPA, LPA+RPA, and the distal vasculature revealed moderate to weak associations with the clinical metrics, signifying the need for *in silico* models based on multiple generations of pulmonary aterial branches. These findings further our understanding of the pulsatile blood flow dynamics in the pulmonary arterial circulation in adult PH and the corresponding relationships between simulation-based hemodynamic indices and standard of care clinical metrics used in the diagnosis and follow up of PH patients.

Supplementary Material

Refer to Web version on PubMed Central for supplementary material.

ACKNOWLEDGMENTS

The use of ANSYS Ensight is gratefully acknowledged through an educational licensing agreement with Ansys, Inc. Computational resources were provided by a Texas Advanced Computing Center (TACC) allocation.

7. FUNDING AND/OR CONFLICTS OF INTERESTS/COMPETING INTERESTS

Research funding was provided in part by National Institutes of Health award No. R01HL121293 and a UTSA Distinguished Research Fellowship (DRF). The content is solely the responsibility of the authors and does not necessarily represent the official views of the National Institutes of Health. The authors have no other conflicts of interest to disclose.

5. REFERENCES

[1]. Galiè N et al. , "Guidelines for the diagnosis and treatment of pulmonary hypertension: the task force for the diagnosis and treatment of pulmonary hypertension of the European society of cardiology (ESC) and the European respiratory society (ERS), endorsed by the international Society of heart and lung transplantation (ISHLT)," European Heart Journal, vol. 30, no. 20, pp. 2493–2537, 2009. [PubMed: 19713419]

[2]. Lai Y-C, Potoka KC, Champion HC, Mora AL, and Gladwin MT, "Pulmonary arterial hypertension: the clinical syndrome," Circulation Research, vol. 115, no. 1, pp. 115–130, 2014. [PubMed: 24951762]

[3]. Reiter G et al. , "Magnetic resonance–derived 3-dimensional blood flow patterns in the main pulmonary artery as a marker of pulmonary hypertension and a measure of elevated mean pulmonary arterial pressure," Circulation: Cardiovascular Imaging, vol. 1, no. 1, pp. 23–30, 2008. [PubMed: 19808511]

[4]. Barker AJ et al. , "Four-dimensional flow assessment of pulmonary artery flow and wall shear stress in adult pulmonary arterial hypertension: results from two institutions," Magnetic Resonance in Medicine, vol. 73, no. 5, pp. 1904–1913, 2015. [PubMed: 24974951]

[5]. Terada M, Takehara Y, Isoda H, Uto T, Matsunaga M, and Alley M, "Low WSS and high OSI measured by 3D cine PC MRI reflect high pulmonary artery pressures in suspected secondary pulmonary arterial hypertension," Magnetic Resonance in Medical Sciences, vol. 15, no. 2, pp. 193–202, 2016. [PubMed: 26567758]

[6]. Kheyfets VO et al. , "Patient-specific computational modeling of blood flow in the pulmonary arterial circulation," Computer Methods and Programs in Biomedicine, vol. 120, no. 2, pp. 88–101, 2015. [PubMed: 25975872]

[7]. Tang BT, Fonte TA, Chan FP, Tsao PS, Feinstein JA, and Taylor CA, "Three-dimensional hemodynamics in the human pulmonary arteries under resting and exercise conditions," Annals of Biomedical Engineering, vol. 39, no. 1, pp. 347–358, 2011. [PubMed: 20640512]

[8]. Yang W, Dong M, Rabinovitch M, Chan FP, Marsden AL, and Feinstein JA, "Evolution of hemodynamic forces in the pulmonary tree with progressively worsening pulmonary arterial hypertension in pediatric patients," Biomechanics and Modeling in Mechanobiology, vol. 18, no. 3, pp. 779–796, 2019. [PubMed: 30635853]

[9]. Kong F, Kheyfets V, Finol E, and Cai XC, "Simulation of unsteady blood flows in a patient-specific compliant pulmonary artery with a highly parallel monolithically coupled fluid-structure interaction algorithm," International Journal for Numerical Methods in Biomedical Engineering, vol. 35, no. 7, p. e3208, 2019. [PubMed: 30989794]

[10]. Piskin S, Patnaik SS, Han D, Bordones AD, Murali S, and Finol EA, "A canonical correlation analysis of the relationship between clinical attributes and patient-specific hemodynamic indices in adult pulmonary hypertension," Medical Engineering & Physics, vol. 77, pp. 1–9, 2020. [PubMed: 32007361]

[11]. Kheyfets V, O'Dell W, Smith T, Reilly J, and Finol E, "Considerations for numerical modeling of the pulmonary circulation—a review with a focus on pulmonary hypertension," Journal of Biomechanical Engineering, vol. 135, no. 6, 2013.

[12]. Bordones AD, Leroux M, Kheyfets VO, Wu YA, Chen CY, and Finol EA, "Computational fluid dynamics modeling of the human pulmonary arteries with experimental validation," Annals of Biomedical Engineering, vol. 46, no. 9, pp. 1309–1324, 9 2018. [PubMed: 29786774]

[13]. Tang BT, Pickard SS, Chan FP, Tsao PS, Taylor CA, and Feinstein JA, "Wall shear stress is decreased in the pulmonary arteries of patients with pulmonary arterial hypertension: an image-based, computational fluid dynamics study," Pulmonary Circulation, vol. 2, no. 4, pp. 470–476, 2012. [PubMed: 23372931]

[14]. Su Z, Hunter KS, and Shandas R, "Impact of pulmonary vascular stiffness and vasodilator treatment in pediatric pulmonary hypertension: 21 patient-specific fluid–structure interaction studies," Computer Methods Programs in Biomedicine, vol. 108, no. 2, pp. 617–628, 2012. [PubMed: 21975085]

[15]. Su Z, Tan W, Shandas R, and Hunter KS, "Influence of distal resistance and proximal stiffness on hemodynamics and RV afterload in progression and treatments of pulmonary hypertension:

a computational study with validation using animal models," Computational Mathematical Methods in Medicine, vol. 2013, 2013.

[16]. Zambrano BA et al. , "Patient-specific computational analysis of hemodynamics and wall mechanics and their interactions in pulmonary arterial hypertension," Frontiers in Bioengineering and Biotechnology, vol. 8, no. 611149, 2021.

[17]. Zambrano BA et al. , "Image-based computational assessment of vascular wall mechanics and hemodynamics in pulmonary arterial hypertension patients," Journal of Biomechanics, vol. 68, pp. 84–92, 2018. [PubMed: 29310945]

[18]. Liu J, Yang W, Lan IS, and Marsden AL, "Fluid-structure interaction modeling of blood flow in the pulmonary arteries using the unified continuum and variational multiscale formulation," Mechanics Research Communications, vol. 107, p. 103556, 2020.

[19]. Vavourakis V, Papaharilaou Y, and Ekaterinaris J, "Coupled fluid–structure interaction hemodynamics in a zero-pressure state corrected arterial geometry," Journal of Biomechanics, vol. 44, no. 13, pp. 2453–2460, 2011. [PubMed: 21762918]

[20]. Gutierrez NG, Kahn A, Burns JC, and Marsden AL, "Computational blood flow simulations in Kawasaki disease patients: insight into coronary artery aneurysm hemodynamics," Global Cardiology Science Practice, vol. 2017, no. 3, 2017.

[21]. Piskin S, Patnaik SS, Han D, Bordones AD, Murali S, and Finol EA, "A canonical correlation analysis of the relationship between clinical attributes and patient-specific hemodynamic indices in adult pulmonary hypertension," Medical Engineering & Physics, vol. 77, pp. 1–9, 2020. [PubMed: 32007361]

[22]. Vachiéry J-L et al. , "Pulmonary hypertension due to left heart diseases," Journal of the American college of Cardiology, vol. 62, no. 25 Supplement, pp. D100–D108, 2013. [PubMed: 24355634]

[23]. Simonneau G et al. , "Haemodynamic definitions and updated clinical classification of pulmonary hypertension," European Respiratory Journal, vol. 53, no. 1, p. 1801913, 2019.

[24]. Kolte D, Lakshmanan S, Jankowich MD, Brittain EL, Maron BA, and Choudhary G, "Mild pulmonary hypertension is associated with increased mortality: a systematic review and meta-analysis," Journal of the American Heart Association, vol. 7, no. 18, p. e009729, 2018. [PubMed: 30371195]

[25]. Robertson E, Choudhury V, Bhushan S, and Walters DK, "Validation of OpenFOAM numerical methods and turbulence models for incompressible bluff body flows," Computers & Fluids, vol. 123, pp. 122–145, 2015.

[26]. Chandra S et al. , "Fluid-structure interaction modeling of abdominal aortic aneurysms: the impact of patient-specific inflow conditions and fluid/solid coupling," Journal of Biomechanical Engineering, vol. 135, no. 8, p. 81001, 2013. [PubMed: 23719760]

[27]. McDonald D, "The relation of pulsatile pressure to flow in arteries," The Journal of Physiology, vol. 127, no. 3, pp. 533–552, 1955. [PubMed: 14368547]

[28]. Weibel ER and Gomez DM, "Architecture of the human lung: use of quantitative methods establishes fundamental relations between size and number of lung structures," Science, vol. 137, no. 3530, pp. 577–585, 1962. [PubMed: 14005590]

[29]. Arzani A, Gambaruto AM, Chen G, and Shadden SC, "Lagrangian wall shear stress structures and near-wall transport in high-Schmidt-number aneurysmal flows," Journal of Fluid Mechanics, vol. 790, pp. 158–172, 2016.

[30]. Finol EA and Amon CH, "Flow-induced wall shear stress in abdominal aortic aneurysms: Part ii-pulsatile flow hemodynamics," Computer Methods in Biomechanics and Biomedical Engineering, vol. 5, no. 4, pp. 319–328, 2002. [PubMed: 12186711]

[31]. Soulis J, Fytanidis D, Seralidou K, and Giannoglou G, "Wall shear stress oscillation and its gradient in the normal left coronary artery tree bifurcations," Hippokratia, vol. 18, no. 1, p. 12, 2014. [PubMed: 25125945]

[32]. Mazzi V et al. , "A Eulerian method to analyze wall shear stress fixed points and manifolds in cardiovascular flows," Biomechanics and Modeling in Mechanobiology, vol. 19, no. 5, pp. 1403–1423, 2019. [PubMed: 31865482]

[33]. Mazzi V, Gallo D, Calò K, Khan M, Steinman D, and Morbiducci U, "A practical approach for wall shear stress topological skeleton analysis applied to intracranial aneurysm hemodynamics,"

in IX Annual Meeting of the European Society of Biomechanics, Bolgona, 2019: Italian chapter of the European Society of Biomechanics.

[34]. Truong U et al. , "Wall shear stress measured by phase contrast cardiovascular magnetic resonance in children and adolescents with pulmonary arterial hypertension," Journal of Cardiovascular Magnetic Resonance, vol. 15, no. 1, p. 81, 2013. [PubMed: 24034144]

[35]. Schäfer M et al. , "Characterization of CMR-derived haemodynamic data in children with pulmonary arterial hypertension," European Heart Journal–Cardiovascular Imaging, vol. 18, no. 4, pp. 424–431, 2017. [PubMed: 27444679]

[36]. Rayz V et al. , "Flow residence time and regions of intraluminal thrombus deposition in intracranial aneurysms," Annals of Biomedical Engineering, vol. 38, no. 10, pp. 3058–3069, 2010. [PubMed: 20499185]

[37]. Papadopoulos KP, Gavaises M, Pantos I, Katritsis DG, and Mitroglou N, "Derivation of flow related risk indices for stenosed left anterior descending coronary arteries with the use of computer simulations," Medical Engineering & Physics, vol. 38, no. 9, pp. 929–939, 2016. [PubMed: 27387905]

[38]. Lee S-W, Antiga L, and Steinman DA, "Correlations among indicators of disturbed flow at the normal carotid bifurcation," Journal of Biomechanical Engineering, vol. 131, no. 6, p. 061013, 2009. [PubMed: 19449967]

[39]. Basciano C, Kleinstreuer C, Hyun S, and Finol E, "A relation between near-wall particle-hemodynamics and onset of thrombus formation in abdominal aortic aneurysms," Annals of Biomedical Engineering, vol. 39, no. 7, pp. 2010–2026, 2011. [PubMed: 21373952]

[40]. Arzani A, "Accounting for residence-time in blood rheology models: do we really need non-Newtonian blood flow modelling in large arteries?," Journal of the Royal Society Interface, vol. 15, no. 146, p. 20180486, 2018.

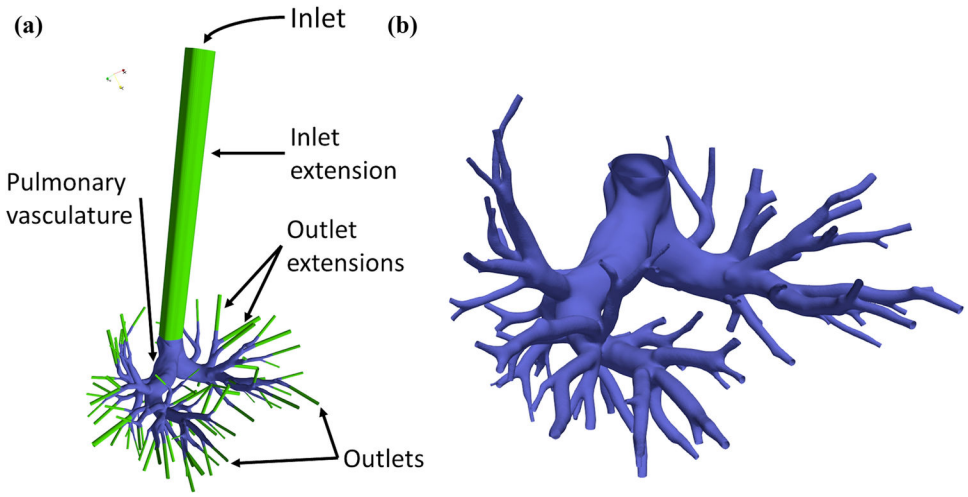

Figure 1:
(a) Schematic of an exemplary patient-specific geometry indicating the inlet, outlet, and wall boundaries. (b) Magnified view of the reconstructed pulmonary vasculature.

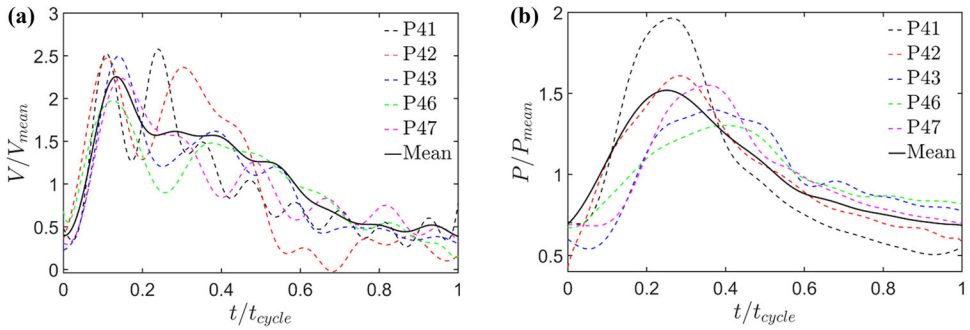

Figure 2:

Normalized centerline (a) velocity, and (b) pressure profiles simultaneously recorded in the proximal MPA for a group of five adult PH patients (labeled as P41, P42, P43, P46, and P47). These patients do not belong to the group of 32 subjects described in Table 2.

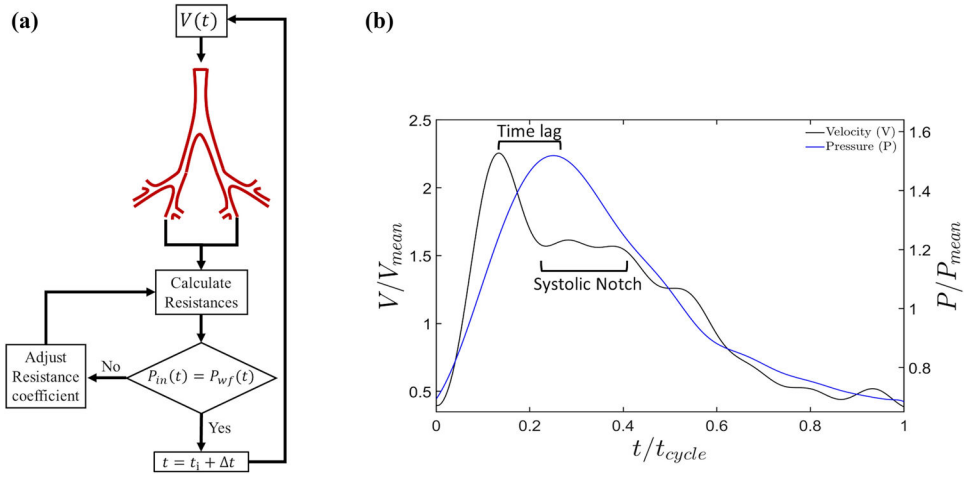

Figure 3:

(a) Schematic of subroutine implemented for simultaneously applying quasi-patient-specific velocity and pressure at the inflow boundary based on imposing outflow resistances. (b) Normalized pressure and velocity waveforms; the velocity waveform distinctively shows the systolic notch characteristic of a PH patient.

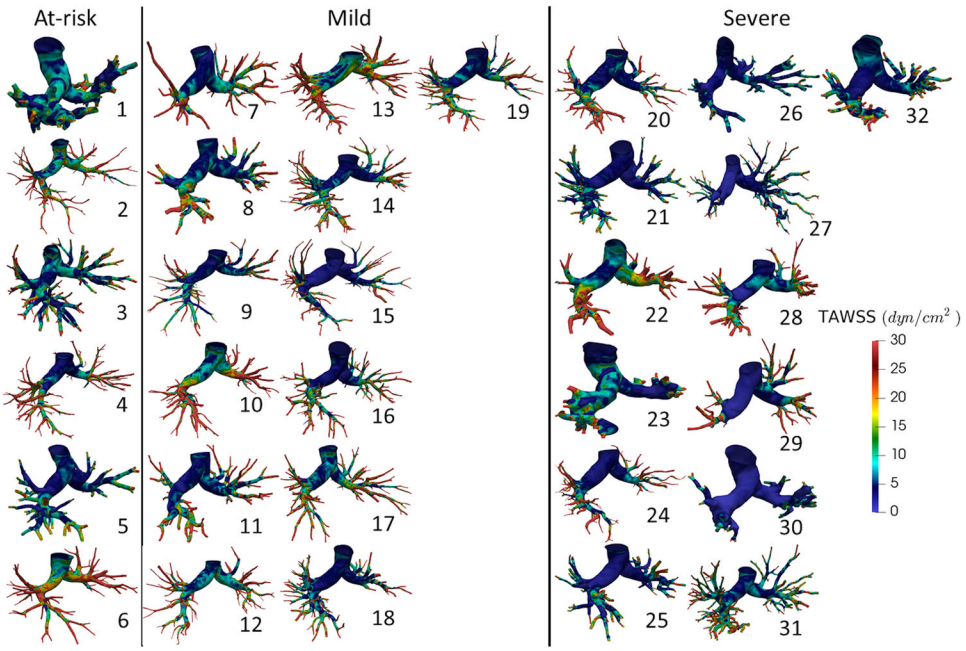

Figure 4:

Time averaged wall shear stress (*TAWSS*) distributions for all patient-specific geometries. Patient numbers are specified next to each stress map. Refer to the corresponding patient number in Table 2 for clinical data collected on each patient.

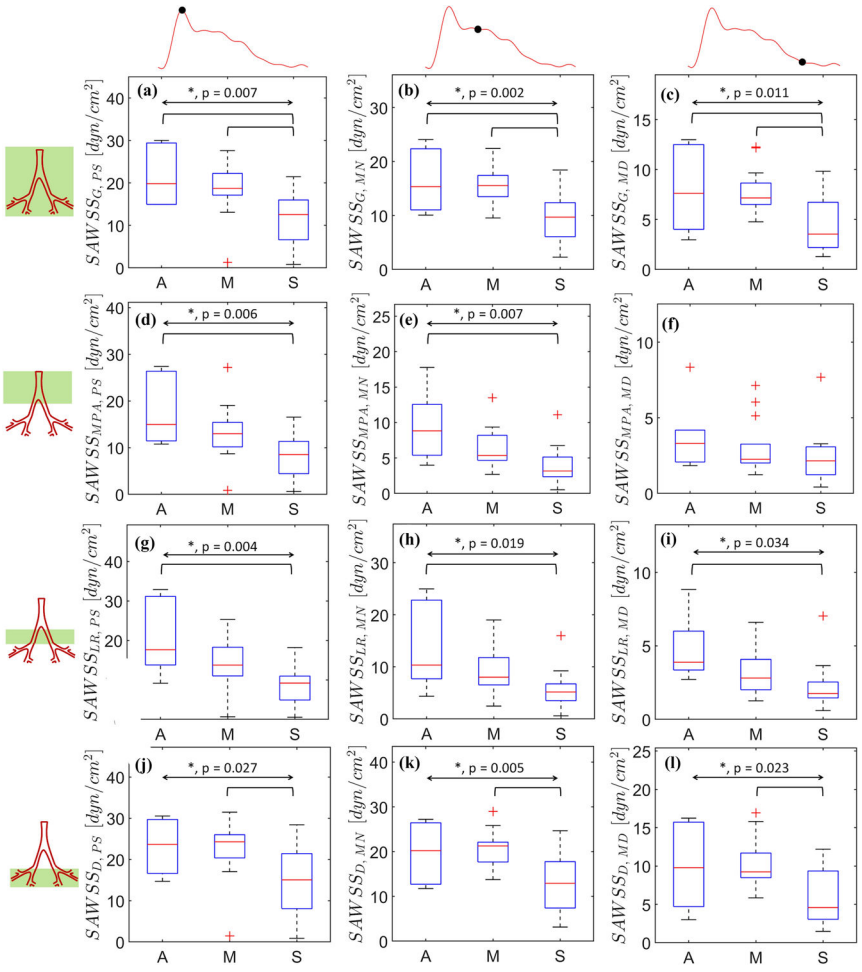

Figure 5:

Spatially averaged wall shear stress (*SAWSS*) calculated at peak systole (a, d, h, j), mid-notch (b, e, h, k), and mid-diastole (c, f, i, l). Region-based spatial averaging is performed in three distinct regions: MPA (d, e, f), LPA+RPA (g, h, i), and the distal vasculature (j, k, l). The overall and pairwise statistical significances are represented by the topmost bidirectional arrow and square brackets underneath, respectively. The crosses represent outliers in each group (*A*, *M*, or *S*).

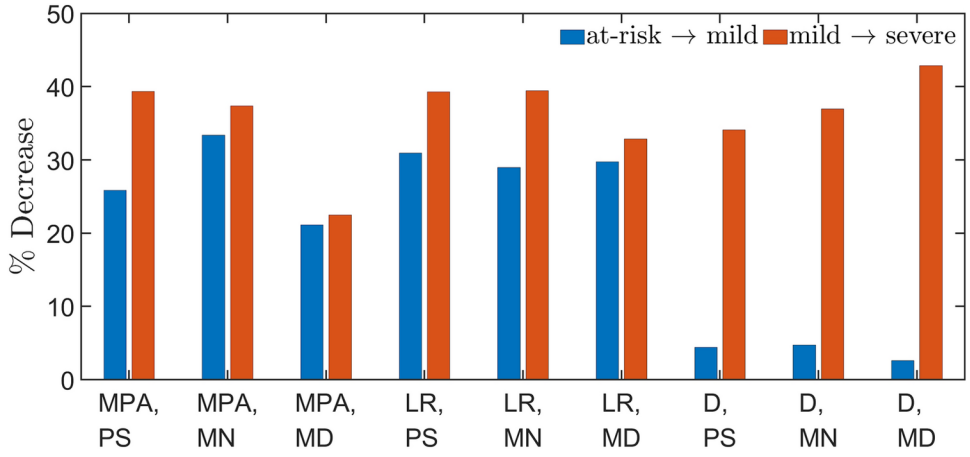

Figure 6:

Percentage decrease in region-wise *SAWSS* between the at-risk (*A*) and mild (*M*) groups, and the *M* and severe (*S*) groups.

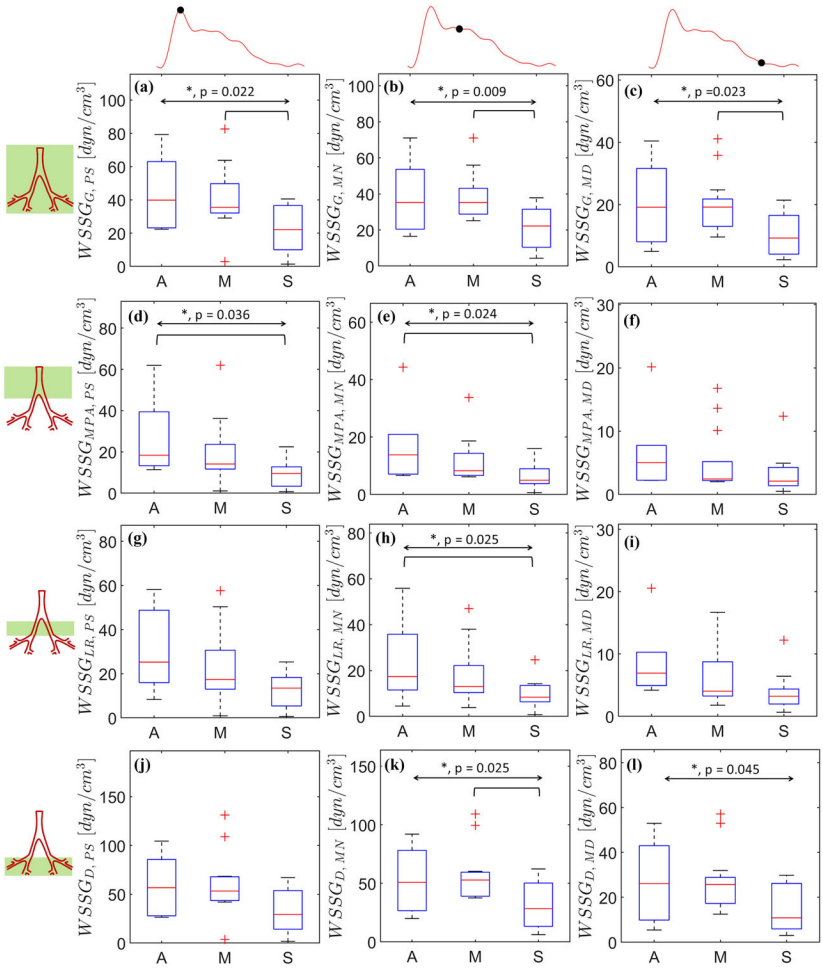

Figure 7:

Spatially averaged wall shear stress gradients (*WSSG*) calculated at peak systole (a, d, h, j), mid-notch (b, e, h, k), and mid-diastole (c, f, i, l). Region based spatial averaging is performed in three distinct regions: MPA (d, e, f), LPA+RPA (g, h, i), and the distal vasculature (j, k, l). The overall and pairwise statistical significances are represented by the topmost bidirectional arrow and square brackets underneath, respectively. The crosses represent outliers in each group (*A*, *M*, or *S*).

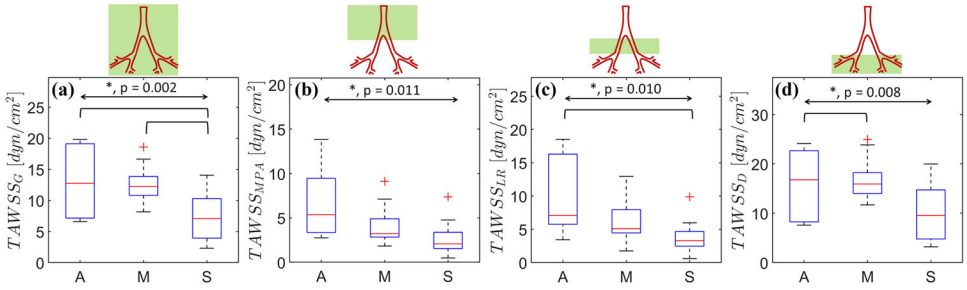

Figure 8:

Time averaged wall shear stress (*TAWSS*) spatially averaged for the (a) complete domain (G), (b) MPA, (c) LPA+RPA (LR), and (d) the distal vasculature (D). The overall and pairwise statistical significances are represented by the topmost bidirectional arrow and square brackets underneath, respectively. The crosses represent outliers in each group (*A*, *M*, or *S*).

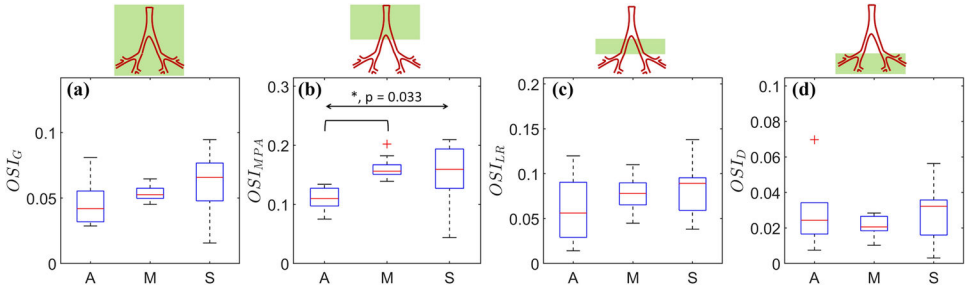

Figure 9:

Oscillatory shear index (*OSI*) spatially averaged for the (a) complete domain (G), (b) MPA, (c) LPA+RPA (LR), and (d) the distal vasculature (D). The overall and pairwise statistical significances are represented by the topmost bidirectional arrow and square brackets underneath, respectively. The crosses represent outliers in each group (*A*, *M*, or *S*).

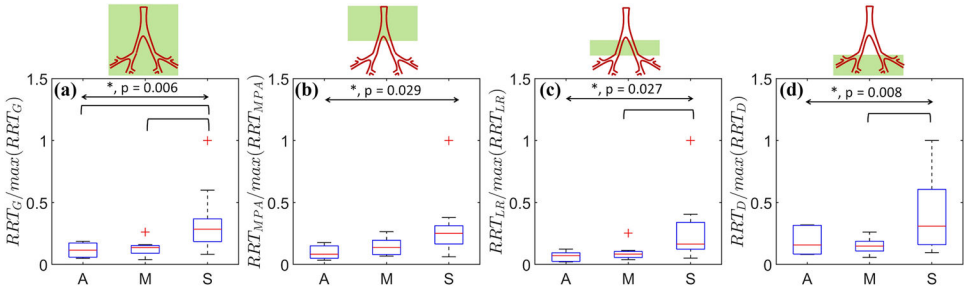

Figure 10:

Normalized relative residence time (*RRT*) spatially averaged for the (a) complete domain (G), (b) MPA, (c) LPA+RPA (LR), and (d) the distal vasculature (D). The overall and pairwise statistical significances are represented by the topmost bidirectional arrow and square brackets underneath, respectively. The crosses represent outliers in each group (*A*, *M*, or *S*).

Table 1:

Abbreviations used in this manuscript with the mathematical expression used for calculations wherever applicable.

Abbreviation	Descriptive form	Remarks
WHO	World Health Organization	
RHC	Right heart catheterization	
SV	Stroke volume	
PVR	Pulmonary vascular resistance	$PVR = (mPAP - PCWP)/CO$
mPAP	Mean pulmonary arterial pressure	$mPAP = (sPAP + 2dPAP)/3$
sPAP	Systolic pulmonary arterial pressure	
dPAP	Diastolic pulmonary arterial pressure	
PCWP	Pulmonary capillary wedge pressure	
C	Compliance	$C = CO/(sPAP - dPAP)$
CO	Cardiac output	$CO = HR \times SV$
HR	Heart rate	
SV	Stroke volume	
SAWSS	Spatially averaged wall shear stress	
WSSG	Wall shear stress gradient	
TAWSS	Time averaged wall shear stress	
OSI	Oscillatory shear index	
RRT	Relative residence time	
RV	Right ventricle	
PA	Pulmonary arteries	
PH	Pulmonary hypertension	

Table 2:

Individual clinical data measured or calculated, retrospectively, from the existing medical records. Refer to Table 1 for a description of all abbreviations. Disease severity is designated as *A* to signify the at-risk (n = 6), *M* to denote mild (n = 13), and *S* to represent the severe (n = 13) PH categories.

Patient No.	Age (*yrs*)	Sex (*M/F*)	Height (*m*)	Weight (*kg*)	WHO group	*PVR* ($N \cdot s/m^5$) × 10^5	*C* (m^3/Pa) × 10^{-3}	*mPAP* (*Pa*) × 10^{-3}	*SV* (m^3) × 10^{-5}	Severity
1	80	F	1.5	92.0	III	153.0	0.4	2.4	8.2	*A*
2	42	F	1.6	75.0	II	136.0	2.0	2.5	7.4	*A*
3	68	F	1.7	77.0	II	151.0	2.3	2.5	8.8	*A*
4	50	M	1.8	65.0	II	158.0	2.9	2.8	5.6	*A*
5	71	M	1.7	95.0	I	120.0	2.8	2.8	7.4	*A*
6	44	F	1.7	90.7	I	143.0	0.0	3.1	7.0	*A*
7	44	F	1.6	104.0	III	285.0	2.0	3.5	7.0	*M*
8	55	F	1.7	95.0	NA	109.0	2.1	3.5	7.2	*M*
9	62	M	1.8	104.0	III	262.0	1.3	3.9	7.6	*M*
10	66	F	1.6	88.0	I	214.0	2.2	3.9	8.8	*M*
11	64	F	1.6	93.0	III	334.0	1.2	3.9	6.7	*M*
12	50	M	1.8	90.0	II	204.0	1.6	4.0	10.5	*M*
13	59	F	1.6	59.0	III	196.0	2.2	4.0	10.8	*M*
14	50	M	1.8	112.0	III	180.0	2.3	4.4	7.4	*M*
15	56	M	1.9	91.0	II	777.0	0.9	4.7	5.4	*M*
16	78	F	1.6	63.0	III	421.0	1.4	4.8	5.8	*M*
17	59	M	1.8	89.0	III	245.0	1.5	5.1	9.5	*M*
18	62	F	1.6	89.0	III	188.0	1.2	5.1	7.7	*M*
19	65	F	1.6	89.0	III	318.0	1.1	5.2	10.1	*M*
20	74	F	1.7	156.0	III	172.0	1.6	5.5	9.0	*S*
21	64	F	1.6	100.0	II	165.0	1.5	5.6	7.4	*S*
22	71	F	1.5	98.0	III	285.0	1.4	5.7	10.5	*S*
23	58	F	1.6	88.0	III	465.0	0.2	5.9	7.2	*S*
24	63	F	1.5	101.0	III	408.0	0.7	6.1	7.1	*S*
25	60	F	1.6	124.0	III	534.0	0.8	6.4	5.9	*S*
26	60	F	1.7	64.0	III	778.0	0.2	6.8	5.1	*S*
27	67	M	1.8	88.0	IV	1316.0	0.4	6.9	4.2	*S*
28	70	M	1.7	67.0	III	906.0	0.7	6.9	5.0	*S*
29	65	M	1.8	82.0	III	745.0	0.5	7.7	6.4	*S*
30	80	M	1.8	93.0	III	830.0	0.2	8.0	6.3	*S*
31	43	M	1.8	63.0	NA	402.0	1.0	8.9	7.5	*S*
32	76	F	1.7	91.0	III	1186.0	0.2	9.3	5.5	*S*

Table 3:

Statistically significant Pearson's correlation coefficients (with Bonferroni correction) obtained between spatially averaged wall shear stress ($SAWSS$) and pulmonary vascular resistance (PVR), compliance (C), and stroke volume (SV).

Simulation based Indices	Pulmonary Vascular Resistance (PVR)	Compliance (C)	Stroke Volume (SV)
$SAWSS_{G,PS}$	−0.52	-	-
$SAWSS_{G,MN}$	−0.67	0.49	0.59
$SAWSS_{G,MD}$	−0.54	-	0.51
$SAWSS_{MPA,PS}$	−0.53	-	0.46
$SAWSS_{MPA,MN}$	−0.57	-	0.61
$SAWSS_{MPA,MD}$	−0.48	-	0.63
$SAWSS_{LR,PS}$	−0.53	-	-
$SAWSS_{LR,MN}$	−0.54	-	0.55
$SAWSS_{LR,MD}$	−0.52	-	0.62
$SAWSS_{D,PS}$	−0.46	0.45	-
$SAWSS_{D,MN}$	−0.62	0.50	0.55
$SAWSS_{D,MD}$	−0.49	-	0.45

Table 4:

Statistically significant Pearson's correlation coefficients (with Bonferroni correction) obtained between spatially averaged wall shear stress gradient (*WSSG*) and pulmonary vascular resistance (*PVR*), compliance (*C*), and stroke volume (*SV*).

Simulation based Indices	Pulmonary Vascular Resistance (*PVR*)	Compliance (*C*)	Stroke Volume (*SV*)
$WSSG_{G,PS}$	−0.46	-	-
$WSSG_{G,MN}$	−0.55	0.47	0.55
$WSSG_{G,MD}$	−0.48	-	0.50
$WSSG_{MPA,PS}$	-	-	0.49
$WSSG_{MPA,MN}$	−0.46	-	0.53
$WSSG_{MPA,MD}$	-	-	0.55
$WSSG_{LR,PS}$	−0.46	-	-
$WSSG_{LR,MN}$	−0.46	-	0.53
$WSSG_{LR,MD}$	−0.45	-	0.59
$WSSG_{D,PS}$	-	-	-
$WSSG_{D,MN}$	−0.50	0.46	0.52
$WSSG_{D,MD}$	-	-	0.47

Table 5:

Statistically significant Pearson's correlation coefficients (with Bonferroni correction) obtained between time averaged wall shear stress ($TAWSS$) and pulmonary vascular resistance (PVR), compliance (C), and stroke volume (SV).

Simulation based Indices	Pulmonary Vascular Resistance (PVR)	Compliance (C)	Stroke Volume (SV)
$TAWSS_G$	−0.62	0.47	0.51
$TAWSS_{MPA}$	−0.51	-	0.51
$TAWSS_{LR}$	−0.52	-	0.49
$TAWSS_D$	−0.56	0.46	0.48

Table 6:

Statistically significant Pearson's correlation coefficients (with Bonferroni correction) obtained between relative residence time (*RRT*) and pulmonary vascular resistance (*PVR*), compliance (*C*), and stroke volume (*SV*).

Simulation based Indices	Pulmonary Vascular Resistance (*PVR*)	Compliance (*C*)	Stroke Volume (*SV*)
RRT_G	0.68	−0.44	−0.51
RRT_{MPA}	0.51	-	-
RRT_{LR}	0.67	-	−0.51
RRT_D	0.65	−0.49	−0.47